fractal and fractional

MDPI

Article

Optically Transparent Dual-Band Metamaterial Absorber Using Ag Nanowire Screen-Printed Second-Order Cross-Fractal Structures

Sumin Bark [1], Junghyeon Kim [1], Minjae Lee [2] and Sungjoon Lim [1,2,*]

[1] School of Intelligent Semiconductor Engineering, Chung-Ang University, Seoul 06974, Republic of Korea; mymini0128@naver.com (S.B.); wjdgus6748@naver.com (J.K.)
[2] School of Electrical and Electronics Engineering, Chung-Ang University, Seoul 06974, Republic of Korea; iamlmj720@gmail.com
* Correspondence: sungjoon@cau.ac.kr

Abstract: In this paper, we propose an optically transparent dual-band metamaterial absorber (MMA) that uses Ag nanowire screen-printed fractal structures. The proposed MMA exhibits near-perfect absorption in the C- and K-bands. This dual-band absorption property is achieved through two inductive–capacitive (L-C) resonances located at 6.45 and 21.14 GHz, which are generated by the second-order fractal structures. We analyzed the microwave absorbing mechanisms through the distributions of the surface current and electromagnetic field on the top and bottom layers. The MMA demonstrates an optical transmittance of 63.1% at a wavelength of 550 nm. This high optical transmittance is attained by screen printing transparent Ag nanowire ink onto a transparent PET substrate. Since screen printing is a simple and low-cost fabrication method, the proposed MMA offers the advantages of being low cost while having the properties of optical transparency and effective dual-band absorption. Consequently, it holds great potential for the radar stealth application of C- and K-bands in that it can be attached to the windows of stealth aircraft due to its optical transparency and dual-band near-perfect absorption property.

Keywords: transparency; screen printing; fractal structure; dual-band adsorption; metamaterial absorber

Citation: Bark, S.; Kim, J.; Lee, M.; Lim, S. Optically Transparent Dual-Band Metamaterial Absorber Using Ag Nanowire Screen-Printed Second-Order Cross-Fractal Structures. *Fractal Fract.* **2024**, *8*, 153. https://doi.org/10.3390/fractalfract8030153

Academic Editors: Viorel-Puiu Paun and Mihai-Virgil Nichita

Received: 27 January 2024
Revised: 3 March 2024
Accepted: 6 March 2024
Published: 8 March 2024

1. Introduction

Electromagnetic absorbers (EAs) are typically employed to mitigate the problem of unwanted electromagnetic waves. The application of EAs has broadened into numerous fields, including defense [1], aeronautics [2], the development of RF anechoic chambers, and electromagnetic shielding technology [3,4]. Traditional EAs (such as pyramidal or tapered-loaded absorbers) rely on a gradual impedance transition, offering the benefit of a wide absorption bandwidth. However, their heavy and bulky nature presents practical constraints, particularly in applications where size and weight are critical (such as in stealth technology). Other conventional EAs include the Salisbury screen [5], the Jaumann absorber [6], and the Dallenbach absorber. However, these types of absorber rely on the destructive interference effect to cancel out the electromagnetic waves, necessitating a thickness that exceeds a quarter of the wavelength of the targeted operating frequency. Therefore, the development of EAs that are both thin and lightweight is crucial for their practical application.

Since Landy et al. experimentally verified the concept of a perfect microwave metamaterial absorber (MMA) in 2008 [7], they have been researched extensively. This interest is largely due to the advantageous properties of MMAs, such as their thin profile and ability to achieve near-perfect absorption. The superior absorption capabilities of MMAs originate from their inductive–capacitive (L-C) resonant structures. However, this electric

and magnetic resonant behavior inherently results in limited bandwidth, restricting their essential application areas. To correct this limitation, researchers have pursued various strategies to expand the bandwidth. A recent study about MMAs utilized a new type of material for a substrate with slotted structure [8]. The two most prevalent techniques include the use of multiple layers within the MMA [9–11] and the integration of various resonant structures within a single unit cell [12–15]. While these methods can broaden the bandwidth, they also increase the absorber's thickness and size, compromising the MMA's inherent advantage of having a thinner and more compact form compared to conventional electromagnetic absorbers.

Since Mandelbrot's original use of the term 'fractal' to describe complex patterns composed of irregular and fragmented shapes [16], fractal geometry has been used in numerous applications across diverse scientific and engineering disciplines. In microwave engineering, fractal structures are employed primarily for two reasons [17–27]. First, their inherent self-similarity enables the activation of multi-band properties without requiring a multilayer construction. Second, the space-filling nature of fractals facilitates more compact designs by optimizing spatial efficiency. Moreover, because the fractal structure is composed of a simple metallic structure, additional lumped element welding is not required. This attribute significantly reduces fabrication costs and streamlines the manufacturing process. Hao et al. [25] demonstrated the use of circular fractal structures when constructing a multi-band MMA with a polarization-insensitive profile. Fang et al. [26] engineered a dual-band MMA that employed fractal designs to achieve stable absorption performance without incorporating any lumped elements. However, despite these advancements, current implementations exhibit limitations in terms of optical opacity. This constraint hinders potential applications in specific scenarios that require simultaneous microwave absorption and visible light transmittance, such as the windows of stealth aircraft or warships.

In the pursuit of expanding the number of applications of MMAs, numerous researchers have attempted to develop a transparent MMA [19,27–33]. The structure of an MMA typically comprises three layers: a conductive resonance layer at the top, an intermediate dielectric layer, and a conductive ground layer at the bottom. The realization of a transparent MMA involves the integration of a transparent substrate, such as glass or polyethylene terephthalate (PET), with a patterned transparent conductor. Among the various candidates for transparent conductors [29,30,34], indium tin oxide (ITO) and silver (Ag) nanowire composites have been validated. In particular, ITO is favored for its optimal balance of transparency and conductivity [19,27,31–33]. Dongyong et al. [19] explored an optically transparent MMA with a second-order cross-fractal structure that employed ITO for the conductive pattern and PET and PMMA as the substrate materials. Hao et al. [33] successfully fabricated a transparent ultra-wideband MMA by using ITO and a substrate comprising PET and polymethylpentene (TPX). Although both of these studies preferred to use ITO, it should be noted that the high cost and complicated fabrication process associated with ITO remains a significant drawback. Additionally, ITO's inherent fragility limits its application in flexible or stretchable contexts. Moreover, employing an intermediate dielectric material with a thickness of several millimeters in the MMA's construction increases the structure's weight, rendering it less suitable for weight-sensitive applications (such as the windows of stealth aircraft).

This paper presents a novel, transparent, dual-band electromagnetic-absorbing metamaterial in which the second-order cross-fractal structure on the top layer enables dual-band near-perfect absorption performance in the C- and K-bands. In addition, the optical transparency of the conductive pattern on the top and bottom substrates is realized through a simple, fast, and cost-efficient method of screen printing with transparent conductive ink embedded with Ag nanowires. Uniquely, the entire substrate of the proposed absorber incorporates an air gap as an intermediate dielectric layer between the top and bottom PET layers for the conductive pattern. This results in a lighter substrate, which is a critical feature in weight-sensitive applications. The previously described advantages render the

proposed MMA a promising candidate for various potential applications within specialized environments, such as the windows of stealth aircraft.

This paper is organized as follows: Section 2 is devoted to the design and analysis processes. After having derived a unit cell of the proposed MMA with second-order cross-fractal structures, an analysis based on electromagnetic mechanisms and parametric study is presented. In Section 3, the fabrication process is considered, detailing the steps of the screen printing process and the logical process used to derive the optimal number of printing cycles. Section 4 presents the experimental test setup and several experimental results regarding the performance of the proposed optically transparent dual-band MMA using second-order cross-fractal structures. Section 5 presents a concise conclusion that summarizes the experimental results and highlights the significance of the paper's content.

2. Design and Analysis

2.1. Design of the Second-Order Cross-Fractal-Structured MMA

Prior research has experimentally demonstrated the various benefits of integrating fractal structures into microwave engineering due to the unique advantages of space filling and self-similarity. These benefits include the expansion of bandwidth through multi-band properties triggered by self-similarity and the size reduction achieved through space filling, making them highly useful for practical applications.

The principles that enable the implementation of multi-band characteristics are as follows. Because patterns of different sizes produce distinct resonance responses, fractal structures composed of self-similar patterns scaled down from the original dimensions can achieve multi-band properties. Among the other fractal structures, the primary advantages of employing second-order cross-fractal structures are that despite their simple structure, it is still feasible for them to have the dual-band properties and TE, TM polarization insensitiveness due to rotational symmetry [26,27,32]. Therefore, in this study, we adopted second-order cross-fractal structures to implement dual-band absorption frequencies for the proposed optically transparent MMA.

The proposed optically transparent MMA has a conventional sandwich structure consisting of three layers: a top conductive pattern, an intermediate dielectric material, and a bottom complete reflection layer. The top conductive pattern layer is a periodic array of second-order cross-fractal-structured unit cells (depicted in Figure 1a). We fabricated a conductive pattern on the top and bottom layers by screen printing transparent conductive ink containing Ag nanowires onto a PET substrate. We selected PET as the substrate material because of its transparency, flexibility, and cost-effectiveness. The measured sheet resistance of each layer was 5.85 and 8.3 Ω/square for the top and bottom, respectively. The dielectric constant and loss tangent of the PET substrate were 3.25 and 0.006, respectively. These values were measured by using a split cylinder resonator (N1501AKEAD-710, EM labs, Kobe, Japan). The side view of the proposed MMA in Figure 1b depicts the layered structure of the substrate with a combination of PET and air. We selected air as the dielectric layer to minimize the weight of the proposed absorber. This choice also helped to enhance the transparency, which was inevitably slightly reduced due to the faint color of the transparent conductive ink which contained the Ag nanowires. Figure 1c shows a 3D view of the full structure of the proposed MMA. We fabricated a frame to maintain an air gap between the top and bottom PET using a 3D printer (3DWOX 7X, Sindoh, Seoul, Republic of Korea).

Figure 1a presents a schematic diagram of the unit structure on the top periodic pattern of the proposed optically transparent dual-band MMA using second-order cross-fractal structures. In the figure, P is the period of the unit cell, and W is the width of both the first-order and second-order cross-fractal structures. In addition, L_1 and L_2 are the lengths of the first-order and the second-order cross structures, t_{PET} is the thickness of the top and bottom PET films, and t_{air} is the thickness of the intermediate air gap.

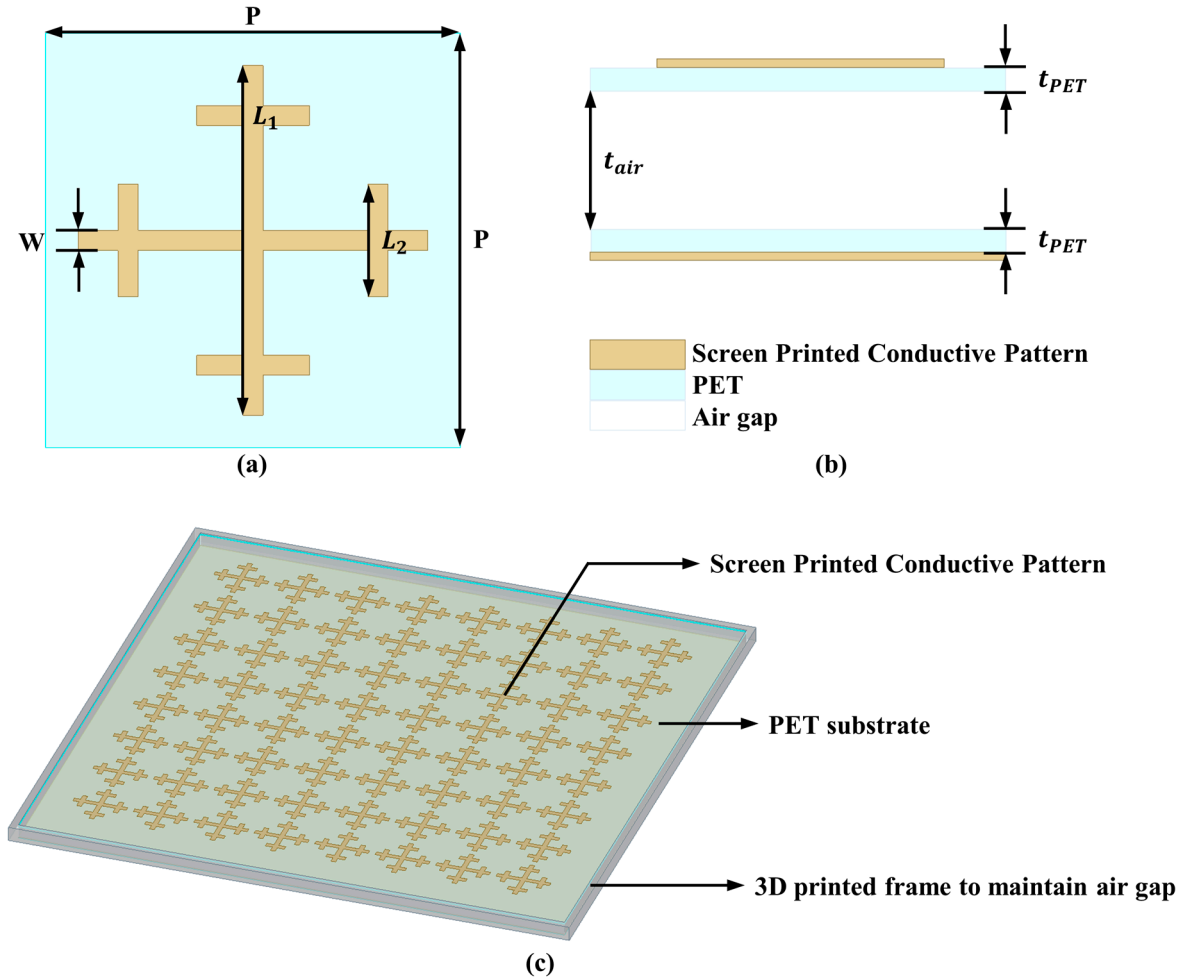

Figure 1. Geometry of the proposed metamaterial absorber (MMA): (**a**) a top view of the unit cell, (**b**) a side view of the unit cell, and (**c**) a 3D view of the full structure.

The three-dimensional electromagnetic simulation software Ansys, a high-frequency structure simulator (HFSS 2016) utilizing the finite element method (FEM), was employed to find the optimum value of the geometric sizes of the unit cell and thickness of each substrate material. To simulate the proposed periodic structure, assuming an infinite periodic structure, we used two pairs of master–slave boundary conditions. We designated the floquet port on the top boundary to generate the incident wave irradiating onto the surface of the proposed MMA. The aim of our optimization process was to achieve two distinct peak frequencies with reflection coefficients of less than −10 dB (one for the C-band and one for the K-band). This goal was based on the expectation that the self-similarity of the second-order cross-fractal structure would excite two absorption peaks. The parameters of the geometric sizes of the unit cell and thickness of each substrate material were optimized through a simulation and are shown in Table 1. The specific optimization process considering the effect on resonant frequency and the absorptivity of each geometric parameter are described in detail in Section 2.2.3. Parametric Study.

Table 1. Dimensions of each geometric parameter.

Parameter	Dimension (mm)	Parameter	Dimension (mm)
P	16.6	L_2	4.5
W	0.8	t_{PET}	0.25
L_1	14	t_{air}	3.4

2.2. Analysis of the Second-Order Cross-Fractal-Structured MMA

2.2.1. Reflection Coefficient, Absorptivity, and Normalized Impedance

The simulated results of the reflection coefficient and absorptivity of the proposed optically transparent dual-band MMA are displayed in Figure 2a. The absorptivity was calculated using Equation (1) [7], where A, S_{11}, and S_{21} are the absorptivity, the reflection coefficient, and the transmission coefficient, respectively.

$$A = 1 - |S_{11}|^2 - |S_{21}|^2 = 1 - |S_{11}|^2 \ (\because S_{21} = 0) \quad (1)$$

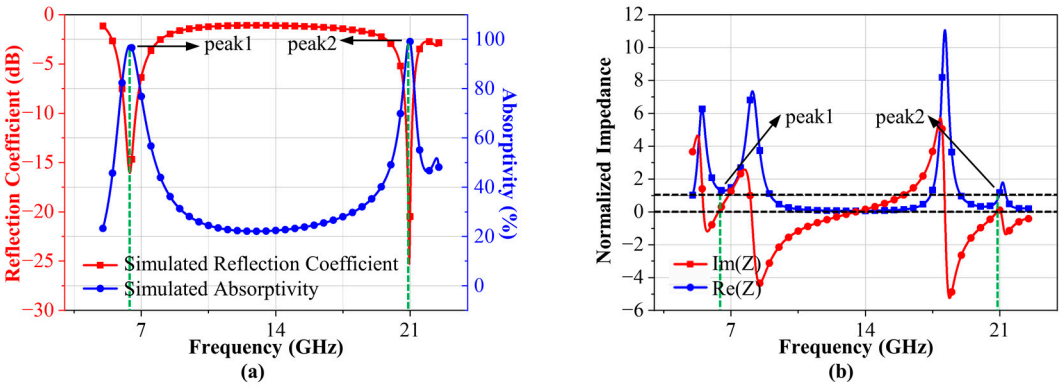

Figure 2. Simulation results of (**a**) the reflection coefficient and absorptivity and (**b**) curves of the real and imaginary parts of the normalized impedance.

Due to the existence of the Ag nanowire screen-printed bottom ground plane for total reflection, the millimeter wave cannot penetrate the absorber, and the transmission coefficient S_{21} is always equal to zero. Therefore, to maximize the absorptivity so that it is greater than 90%, the reflection coefficient from the top plane of the proposed absorber should be minimized to less than −10 dB. As expected from the property of the second-order cross-fractal structure, two absorption peaks were evident at 6.40 and 20.96 GHz, with reflection coefficients of −16.04 and −25.26 dB, respectively. With regard to absorptivity, the lower peak was 97.5%, while the higher peak exhibited an absorptivity of 99.7%. The performance of the proposed absorber, in terms of absorbing waves, depends on two key factors. First, impedance matching between the electromagnetic absorber and free space is crucial. This matching primarily determines the extent of reflection at the absorber's surface. The other factor is the loss characteristic of the absorber, which results in electromagnetic power attenuation.

Figure 2b displays curves of the real and imaginary parts of the normalized impedance of the proposed optically transparent dual-band MMA. The normalized intrinsic impedance Z was calculated using Equation (2) [11], where Z_M and Z_0 are the intrinsic impedances of the proposed MMA and free space (377 Ω).

$$Z = \frac{Z_M}{Z_0} = \frac{\sqrt{(1+S_{11})^2 - {S_{21}}^2}}{\sqrt{(1-S_{11})^2 - {S_{21}}^2}} = \frac{1+S_{11}}{1-S_{11}} \ (\because S_{21} = 0) \quad (2)$$

The real part of the normalized impedance was close to 1 at the two absorption peaks of 6.40 and 20.96 GHz, which indicated that the characteristic impedance of the designed electromagnetic absorber was nearly equal to the impedance in free space at the two aforementioned peak frequencies of 6.40 and 20.96 GHz. The imaginary part of the normalized impedance was close to 0 at the two absorption peaks at 6.40 and 20.96 GHz. This result indicated that the phase difference between the electric and magnetic field components at the interface between the designed electromagnetic absorber and free space was close to 0 at the two aforementioned peak frequencies.

2.2.2. Analysis of Electromagnetic Absorption Mechanism

We conducted detailed numeric simulations to demonstrate the physical mechanism of wave absorption of the proposed optically transparent dual-band MMA. The aim was to obtain detailed distributions of the surface current and the electric field, as displayed in Figures 3 and 4.

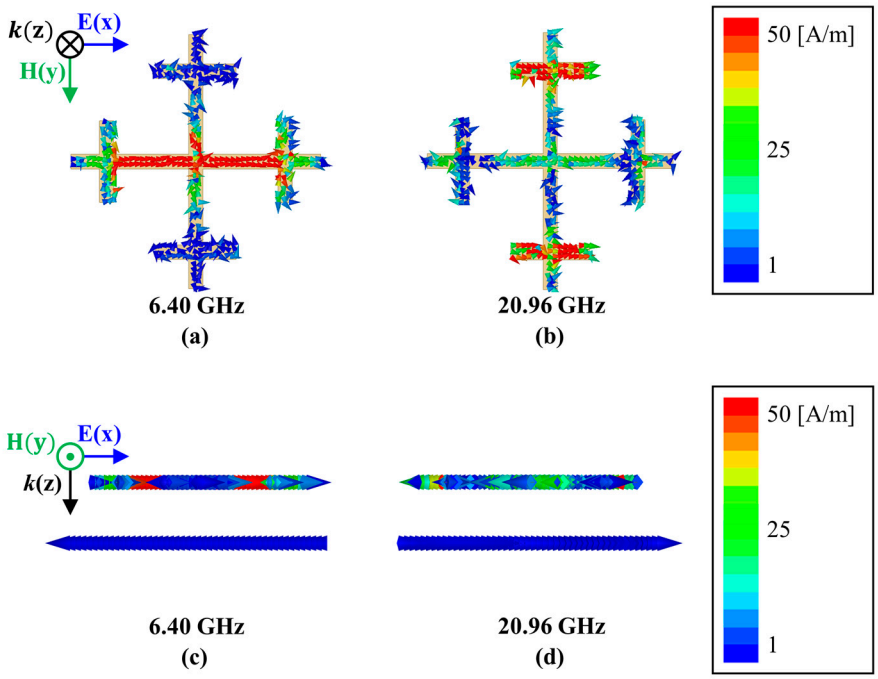

Figure 3. Simulation results of the surface current (**a**) at 6.40 GHz on the top fractal pattern and (**b**) at 20.96 GHz on the top fractal pattern. Side view of the simulated surface current (**c**) at 6.40 GHz and (**d**) at 20.96 GHz.

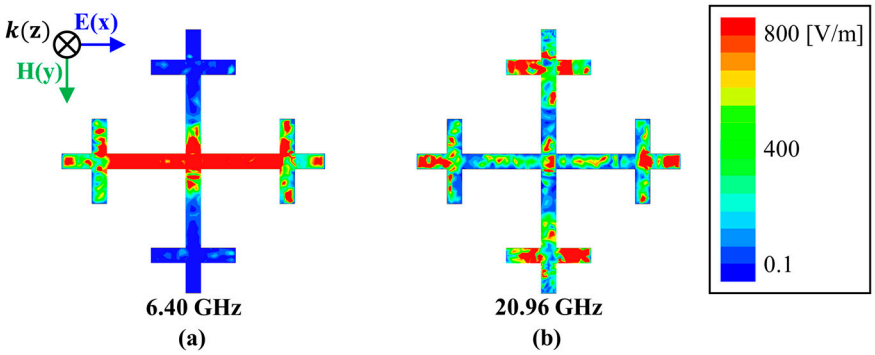

Figure 4. Simulation results of the electric field distribution (**a**) at 6.40 GHz on the top fractal pattern and (**b**) at 20.96 GHz on the top fractal pattern.

In Figure 3, the arrows indicate the direction of the current flow, and the varying colors indicate the current intensity levels. Figure 3a reveals that there was a significant surface current on the larger cross structure at the center of the top layer at 6.40 GHz. This finding confirmed that the peak absorption frequency of 6.40 GHz was directly related to the larger cross pattern which is the first-order cross structure. As depicted in Figure 3b, significant surface current was evident on the smaller cross patterns at the edges of the top layer at 20.96 GHz. This result suggested that the higher peak absorption frequency of 20.96 GHz was related to the smaller cross pattern which is the second-order cross structure.

Figure 3c,d display the distribution of surface current on the top and the bottom layers of the proposed absorber from the side view. As demonstrated in both (c) and (d),

we can find one common observation that the directions of the surface current on the top and bottom layers were reversed and parallel. The surface current on the top fractal pattern layer and the bottom ground layer were in an anti-parallel relationship, forming a closed-ring current. These current loops resulted in a strong magnetic coupling resonance, which played a critical role in the highly efficient absorption at the resonant frequencies of 6.40 and 20.96 GHz.

Figure 4 displays the electric field distribution characteristics of the top second-order cross-fractal pattern. In the figure, the varying colors indicate the intensity levels of the field. As depicted in Figure 4a, the electric field of the top fractal pattern at 6.40 GHz was concentrated at the larger cross pattern at the center. This was because the surface current of the top fractal pattern was concentrated on the first-order cross structure. As depicted in Figure 4b, the electric field of the top fractal pattern at 20.96 GHz was concentrated on the smaller cross patterns at the edges. This was due to the distributions of the surface current being concentrated on the second-order cross structure at 20.96 GHz, as displayed in Figure 3b.

By analyzing the distributions of the surface current and the electric field in the proposed absorber structure, we demonstrated the mechanism that explained the connection between the second-order cross-fractal structure and its dual-band near-perfect absorption property.

2.2.3. Parametric Study

In this work, we conducted several parametric studies to figure out the effects on RF performance, such as absorption frequency and absorptivity, that each geometric parameter has. Based on this parametric analysis, we could effectively determine the optimum value of each parameter so that the proposed MMA could realize the performance we intended. In addition, through parametric study, we can analyze whether a simulated result is convincing enough or not, meaning that it acts as a guide to analyzing unexpected phenomena while designing.

We found out that two parameters, namely L_1 and L_2, among the six geometric parameters given in Table 1 have a major influence on the resonant frequency. Each parameter was changed independently without changes in all other conditions. The result for changing the length of the first-order cross pattern from 13.5 to 14.5 mm is shown in Figure 5a,b. The result for changing the length of second-order cross pattern from 4.0 to 5.0 mm is shown in Figure 5c,d. To show the frequency shift more clearly, it is essential to show the smaller span of frequency than a larger span that shows both lower and higher peaks. Therefore, the results within the lower-frequency range and higher-frequency range are given, respectively.

It is shown in Figure 5a that as the length L_1 increased from 13.5 to 14.5 mm, the absorption peak frequency in the lower-frequency range gradually decreased from 6.57 to 6.26 GHz. Similarly, as shown in Figure 5b, the absorption frequency in the higher-frequency range decreased from 21.11 to 20.77 GHz. It is shown in Figure 5c that as the length L_2 increased from 4.0 to 5.0 mm, the absorption peak frequency in the lower-frequency range gradually decreased from 6.60 to 6.22 GHz. Similarly, as shown in Figure 5d, the absorption frequency in the higher-frequency range decreased from 21.19 to 20.67 GHz. This is due to the increasing effective inductance owing to the increasing length of the pattern. When the effective inductance increases, resonant frequency, which refers to the absorption frequency in the MMA, decreases based on Equation (3) [35], where L represents the effective inductance, and C represents the effective capacitance.

$$f_r = \frac{1}{2\pi\sqrt{LC}} \tag{3}$$

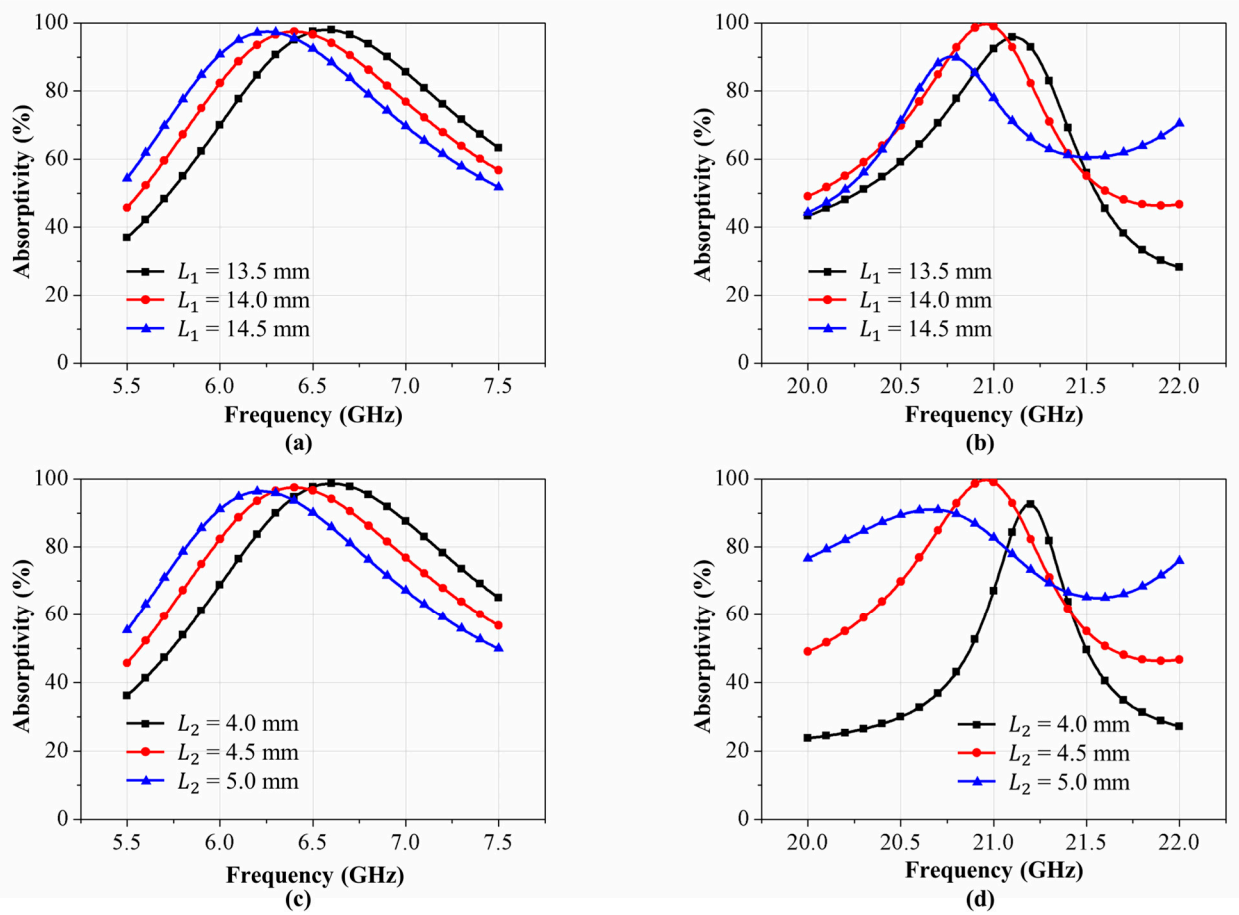

Figure 5. Simulated absorptivity according to frequency with varying lengths of the first-order cross pattern, L_1, in a (**a**) lower-frequency range and (**b**) a higher-frequency range; simulated absorptivity according to frequency with varying lengths of the second-order cross pattern, L_2, in a (**c**) lower-frequency range and (**d**) a higher-frequency range.

In Section 2.2.2, we concluded that the larger cross pattern, the first-order cross pattern, is related to the lower absorption peak, and the smaller cross pattern, the second-order cross pattern, is related to the higher absorption peak. However, as shown in Figure 5, changing the lengths of larger or smaller patterns affects both the lower and higher peak frequencies. This phenomenon may, at first, appear to contradict the conclusions previously drawn, but it is due to the characteristic of the second-order cross-fractal structure. The reason why changing both lengths has the effect of a frequency shift on both the lower- and higher-frequency ranges is the overlap between the edges of both the larger cross pattern and the smaller cross pattern.

Our analysis revealed that among the six geometric parameters listed in Table 1, two specific parameters, namely W and t_{air}, play a critical role in the matching the impedance between the proposed metamaterial absorber (MMA) and air. This, in turn, significantly impacts the absorptivity of the proposed MMA.

Figure 6a shows the simulated absorptivity with varying W, the width of the pattern, from 0.6 to 1.0 mm. The peak absorptivity for widths of 0.6, 0.8, and 1 mm was 92.64%, 97.52%, and 99.67%, respectively. This shows that the absorptivity slightly increased as the width of the pattern increased. This can be demonstrated through the impedance matching between the proposed MMA and the air. Figure 6b shows curves of the real and imaginary values of the normalized impedance with increasing pattern width. It is shown that as W increased, the real value of the normalized impedance became closer to 1 and the imaginary value of the normalized impedance became closer to 0, which indicates perfect impedance

matching. Through this result, we can observe the trend of the larger the width, the larger the absorptivity, as well as the fact that a width of 1.0 mm showed almost perfect absorption. However, we chose 0.8 mm for the width of the absorber to fabricate the screen printing mask. This decision aimed to consider a fabrication error from the screen printing process near 0.2 mm. The result possibly caused by this decision is that due to the fabrication error, the fabricated prototype shows absorptivity from 97 to 99%, which is the simulated peak absorptivity for a width between 0.8 and 1.0 mm.

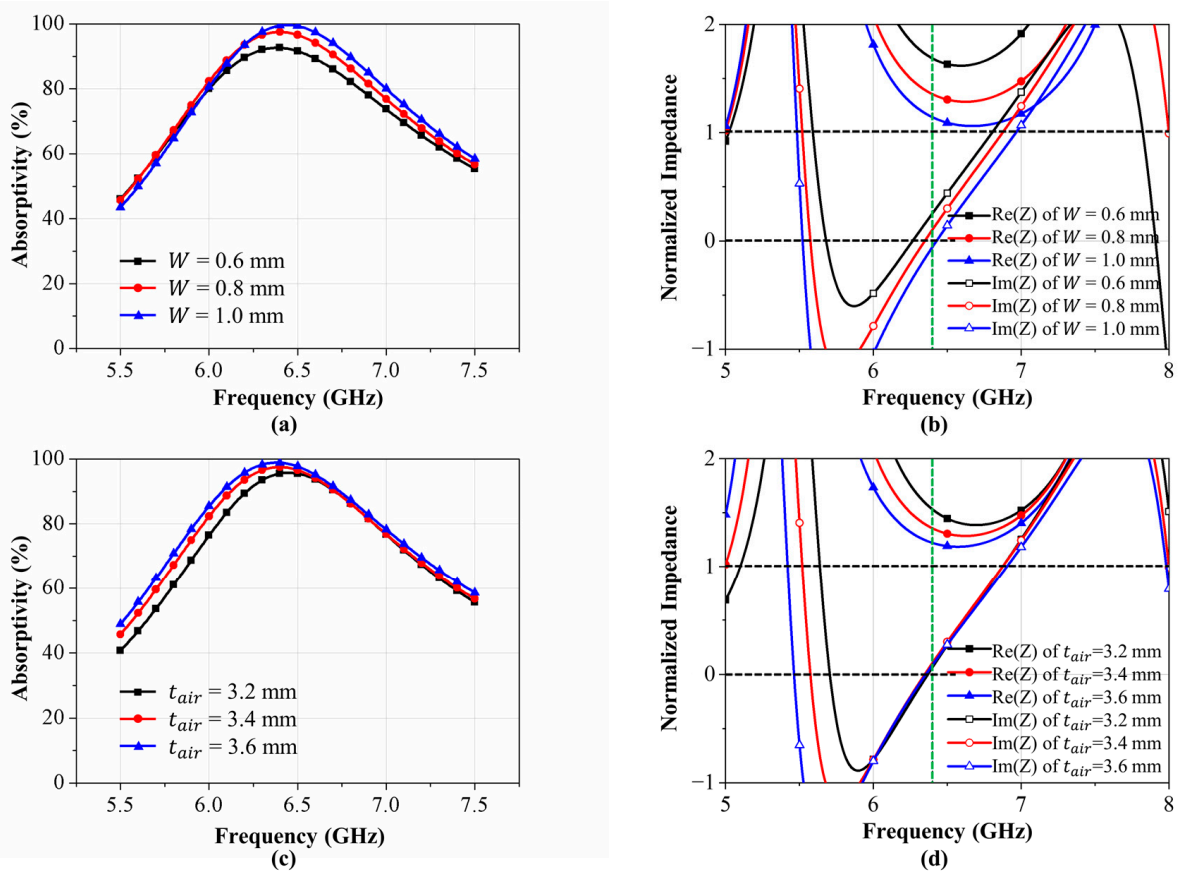

Figure 6. Simulation results of (**a**) absorptivity and (**b**) curves of the real and imaginary parts of the normalized impedance with varying pattern widths; simulation result of (**c**) absorptivity and (**d**) curves of the real and imaginary parts of the normalized impedance with varying air gap thicknesses.

Figure 6c shows the simulated absorptivity with varying t_{air}, the thickness of the air gap, from 3.2 to 3.6 mm. The peak absorptivity for thicknesses of 3.2, 3.4, and 3.6 mm was 95.77%, 97.52%, and 98.88%, respectively. This shows that the absorptivity slightly increased as the thickness of the air gap increased. Similarly, this can be demonstrated through the impedance matching between the proposed MMA and the air. Figure 6b shows curves of the real and imaginary values of the normalized impedance with increasing t_{air}. It is shown that as t_{air} increased, the real value of the normalized impedance became closer to 1 and the imaginary value of the normalized impedance became closer to 0, which indicates perfect impedance matching. Through this result, we can observe the trend of the larger the thickness of the air gap, the larger the absorptivity, as well as the fact that a thickness of 3.6 mm showed almost perfect absorption. However, we chose 3.4 mm for the thickness of the 3D-printed frame to maintain a certain thickness of air gap. This decision aimed to consider a fabrication error from the 3D printing process. The result possibly caused by the decision is that due to the fabrication error, the fabricated prototype shows absorptivity from 97 to 99%, which is the simulated peak absorptivity for t_{air} between 3.2 and 3.4 mm.

3. Fabrication

In this study, we screen printed transparent conductive ink embodied with Ag nanowires to fabricate the proposed optically transparent dual-band MMA. Screen printing is a stencil-based printing technique where ink is applied to the printing surface only through the stencil areas of the design. Screen printing techniques continue to be widely used not only in art and clothing manufacturing but also in various engineering fields, even though they were developed over 100 years ago. This is on account of the advantages of these techniques, including their uncomplicated process, rapid production speed, and low cost. Accordingly, with just a screen printing mask and modest facilities, it is possible to generate a large number of prints quickly. Therefore, the decision to use the screen printing technique as a fabrication method was driven by the aim to enhance the practical applicability of the absorber, leveraging its low cost, simplicity, and compatibility with large-scale manufacturing processes.

Figure 7 displays the entire screen printing process, including sintering and the repeated printing cycle. We used DM-SNW-8012S (DYCOTEC Materials, Calne, UK), which is a transparent conductive ink containing Ag nanowires. We opted for a screen printing mask constructed from a P120 screen mesh featuring an emulsion thickness of 21 µm because this configuration was optimal for the ink used. The suggested printing speed ranges from 70 to 400 mm/s. Our printing was conducted at 150 mm/s using an auto-align screen printer (SJ-7320SA, Sungjin Technology, Gimhaae, Republic of Korea). Enhancing the conductivity of the Ag nanowire ink requires a post-printing step, such as thermal sintering. This common technique helps to fuse the junctions of the Ag nanowires, boosting conductivity. Accordingly, we cured the printed layers at 140 °C for 20 min in an oven.

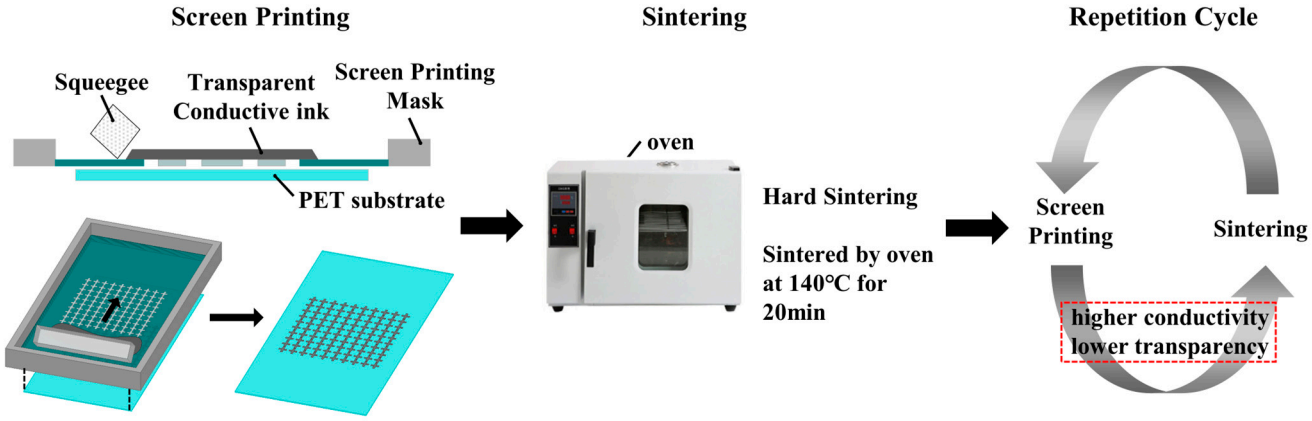

Figure 7. Screen printing and sintering processes.

The conductivity of a pattern printed once with this ink was insufficient for the fabrication of an electromagnetic absorber with an absorptivity of greater than 90%. We resolved this problem through repeated screen printing cycles. The conductivity improved with each additional printing cycle, although this caused decreased transparency. Since there was a trade-off between conductivity and transparency in the printed pattern, it was crucial to determine the optimal number of printing cycles to achieve an MMA that balanced high absorptivity with optical transparency.

We conducted parametric simulations in which the sheet resistance of the top pattern and bottom ground of the proposed unit cell structure were varied to determine the minimum sheet resistance that enables an absorptivity of greater than 90%. As depicted in Figure 8a, the absorptivity of the proposed absorber with varying sheet resistance increases approximately linearly as the sheet resistance decreases. To realize an absorptivity of greater than 90%, a sheet resistance of less than 10 Ω/square is required.

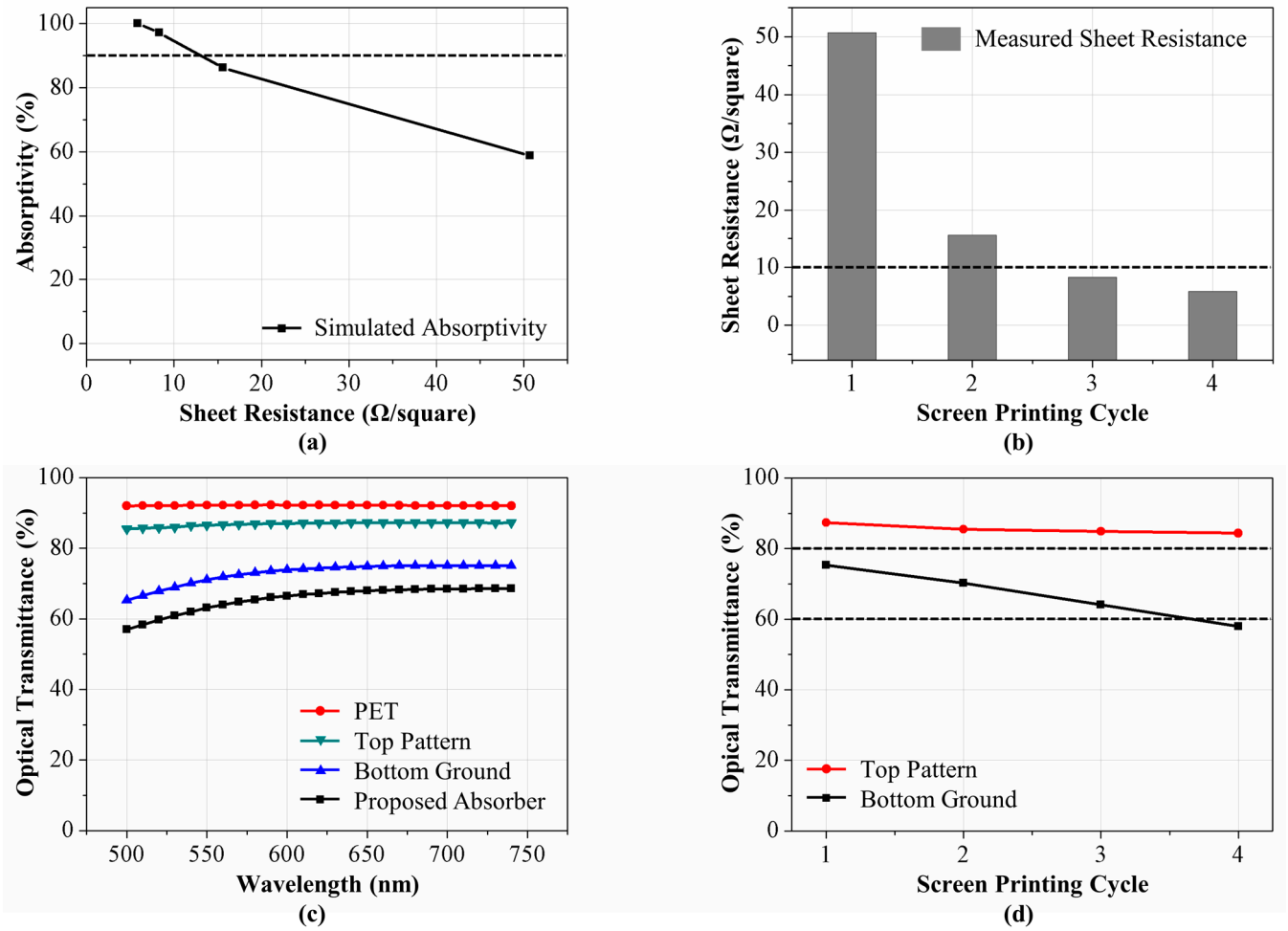

Figure 8. (**a**) Simulated absorptivity for conductive patterns with varying sheet resistances on the top and bottom layers of the proposed absorber; (**b**) sheet resistance measured across different cycles of screen printing; (**c**) optical transmittance measured for various specimen types; (**d**) optical transmittance measured at a wavelength of 550 nm across various screen printing cycles.

Figure 8b displays the sheet resistance measurements for the Ag nanowire pattern printed via screen printing over several cycles. The sheet resistances of each cycle, from 1 to 4, were 50.7, 15.6, 8.3, and 5.85 Ω/square, respectively. Achieving a sheet resistance of less than 10 Ω/square, which is necessary for realizing an absorptivity of greater than 90%, required a minimum of three printing cycles.

The proposed optically transparent dual-band MMA consisted of three layers: a top screen-printed conductive fractal pattern on the PET, a bottom screen-printed conductive ground on the PET, and an intermediate air gap. Figure 8c displays the measured optical transmittance of four specimens: the PET material without any patterns, the top layer, the bottom layer, and the proposed absorber. The optical transmittance was measured using a spectrophotometer (CM-36dG, KONICA MINOLTA, Tokyo, Japan). A notable finding that can be seen in Figure 8c is that the optical transmittance of the bottom ground layer was the primary factor influencing the optical transmittance of the proposed absorber.

We measured the optical transmittance of eight specimens: four top patterns with 1–4 repeated printing cycles and four bottom grounds with 1–4 repeated printing cycles. Figure 6d displays the optical transmittance data at a wavelength of 550 nm (representing the middle of the visible spectrum) for the eight samples. As the number of printing cycles increased, the optical transmittance decreased. Notably, the optical transmittance of the bottom ground layer, which is a critical factor affecting the transparency of the proposed absorber, reduced to less than 60% after more than four printing cycles.

From Figure 8a,b, we concluded that three or more printing cycles were required to achieve an absorptivity exceeding 90%. However, Figure 8c,d demonstrate that to attain an optical transmittance exceeding 60% for the crucial bottom ground layer, which serves as the bottleneck for the overall optical transmittance of the absorber structure, only three or fewer printing cycles were required. Therefore, we logically inferred from these data that the optimal number of screen printing cycles to fabricate the bottom ground layer was three. Additionally, for the top pattern, which is not a primary factor influencing the optical transmittance of the entire structure, we selected four printing cycles to decrease the sheet resistance of the printed pattern, thereby increasing the absorptivity of the proposed absorber.

Figure 9 exhibits a fabricated prototype of the suggested optically transparent dual-band MMA using Ag nanowire screen-printed second-order cross-fractal structures. We placed unit cells in 8×8 arrays and implemented a full structure with a size of 150×150 mm^2, as displayed in Figure 8a. Figure 8b presents an image taken in an outdoor environment to verify the transparency of the fabricated prototype. A comparison between Figure 8b,c highlights that the fabricated prototype could potentially be attached to windows in diverse settings. This prototype could be used for electromagnetic wave absorption or electromagnetic shielding without impairing the windows' transparency, seamlessly blending in with the surroundings.

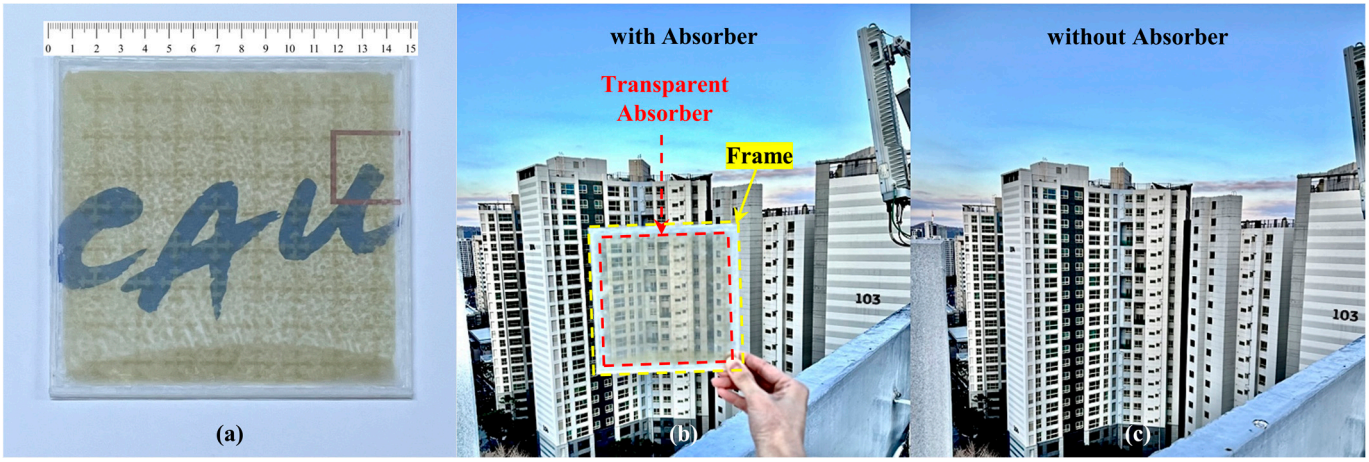

Figure 9. (**a**) Photograph of the fabricated prototype of the proposed absorber. Comparative photographs demonstrating the transparency of the proposed absorber via (**b**) an image taken with the absorber present and (**c**) an image taken without the absorber in place.

4. Results and Discussion

Figure 10 illustrates the far-field testing setup used for measuring the reflection coefficient of the fabricated prototype. To measure the absorption located in the lower-frequency range, a horn antenna (GH1-18N, Dorado International, Tukwila, WA, USA) with an operating frequency range of 1–18 GHz and a nominal gain of 6–10 dB was used, whereas to measure the absorption located in the higher-frequency range, a horn antenna (CMI-220HA20, Quantic Corry, Cranberry Township, PA, USA) with an operating frequency range of 18–26.5 GHz and a nominal gain of 20 dB was used. The distance between the proposed MMA and the horn antenna, which satisfies the far-field condition that a radiation pattern of the wave from the horn antenna does not change, was calculated using Equation (4) [36], where d is the far-field distance, D is the dimension of the horn antenna, and λ is the wavelength of the target frequency. D for an antenna operating in a lower-frequency range was 290.7 mm; therefore, d for low-frequency measurement setup was 3.60 m. Likewise, as D for antenna operation in a higher-frequency range was 80.43 mm, d for the high-frequency measurement setup was 0.9 m.

$$d = \frac{2D^2}{\lambda} \tag{4}$$

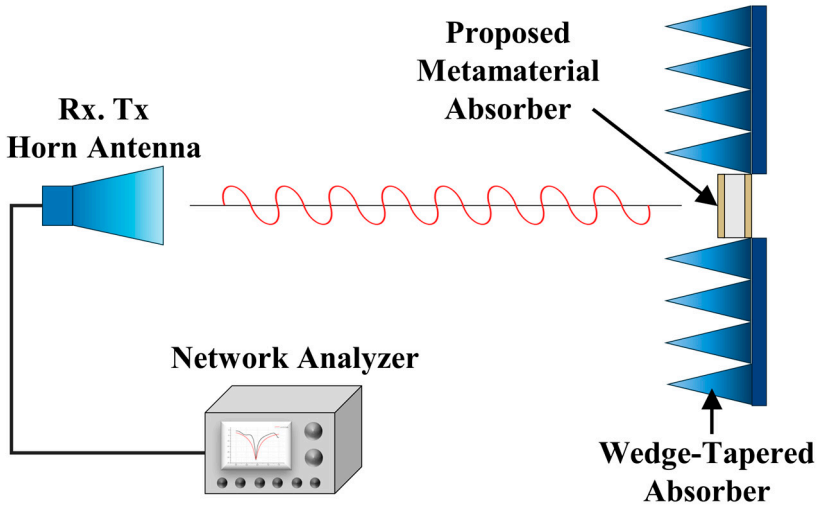

Figure 10. Photograph of the experimental test setup for the reflection coefficient measurement.

The wedge-tapered absorber was placed to absorb and block electromagnetic waves that were reflected from the surrounding environment. A single horn antenna served as both the transmitting and receiving antenna. To avoid reflections from the ground floor, the horn antenna was placed on tall holders. A Keysight network analyzer was used to measure the reflection coefficient. We employed the time-gating technique of the network analyzer to isolate and identify the specific electromagnetic wave that was reflected solely from the absorber prototype. Before measuring the S_{11} of the prototype, a copper plate of the same size was measured for calibration, because the reflection coefficient of the copper plate is the standard of $|\Gamma| = 1$. Therefore, the calibration process was carried out by subtracting the S_{11} of the coper plate from the S_{11} of the prototype. Then, the absorptivity of the proposed absorber was calculated using Equation (1), substituting the calibrated value, which is the result of the subtraction, as the S_{11} in Equation (1). As mentioned previously, the S_{21} of the prototype was expected to be zero because of the complete reflection occurring at the bottom screen-printed ground layer of the proposed MMA.

Figure 11 displays the S-parameter measurement result of the proposed optically transparent dual-band MMA using an Ag nanowire screen-printed second-order cross-fractal structure. Figure 9a,b compare the measurement and simulation results at the lower- and higher-frequency ranges, respectively. The simulated lower absorption peak was at 6.40 GHz, with an absorptivity of 97.51%, while the measured lower absorption peak was at 6.45 GHz, with an absorptivity of 97.48%. The simulated higher absorption peak was at 20.96 GHz, with an absorptivity of 99.70%, while the measured higher absorption peak was at 21.14 GHz, with an absorptivity of 98.92%. Although there was a frequency shift of 0.18 GHz in the higher-frequency range, the tested value agreed well with the simulated values within an allowable error range. The fact that the simulation results of the infinite periodic structure are similar to the measurement results indicates that the 3D-printed frame structure designed to maintain the air gap located at the edge of the periodic structure does not have a significant impact on RF performance. This result proved the correctness and credibility of the simulation model. As depicted in Figure 11b, for both the C- and K-bands, there were highly effective absorption bands in which the reflection coefficient remained at less than -10 dB and the absorptivity exceeded 90%. Consequently, we could conclude that the dual-band property resulting from the second-order cross-fractal structured unit cell had been experimentally demonstrated. The measured optical transmittance also revealed that the suggested optically transparent MMA allowed for 63.1% of light to transmit at a wavelength of 550 nm, which is the midpoint of the visible light spectrum.

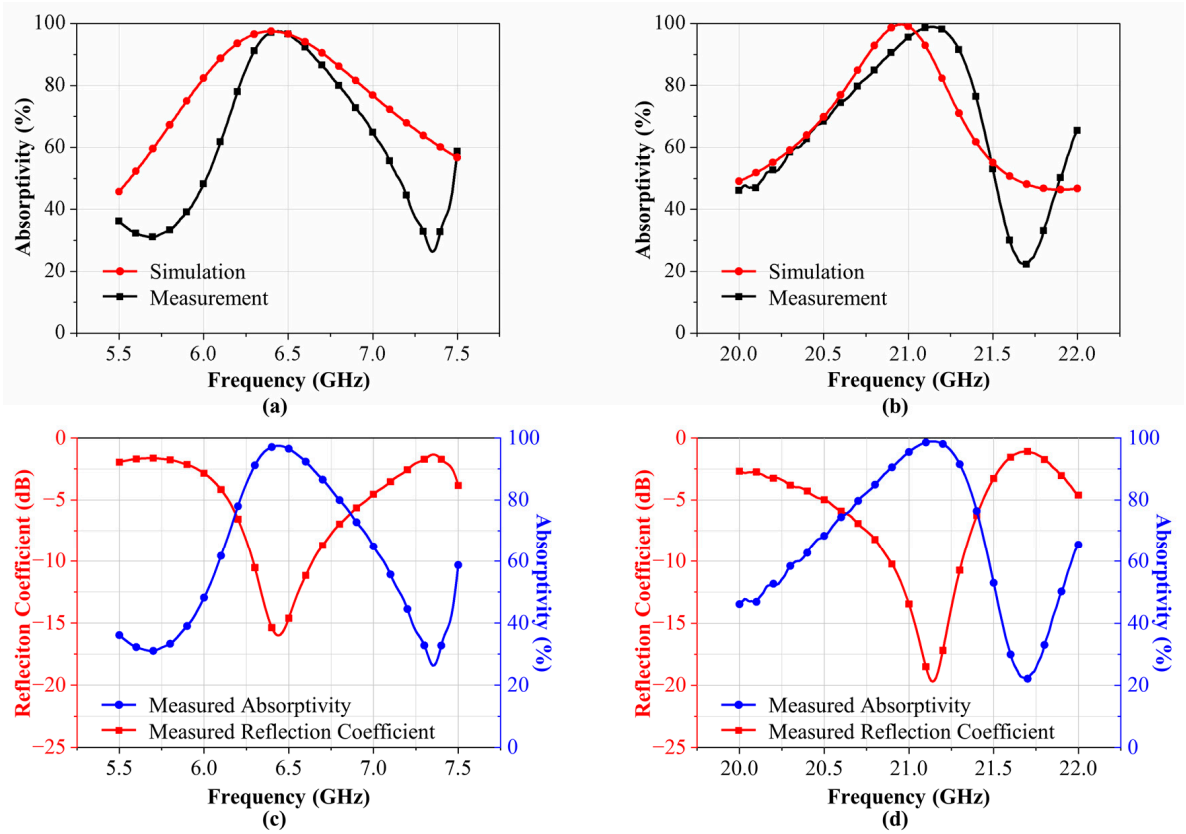

Figure 11. Comparative analysis of the measured and simulated absorptivity results for the proposed MMA in (**a**) the lower-frequency range and (**b**) the higher-frequency range; measurement of the reflection coefficient and absorptivity for the proposed MMA at (**c**) the lower-frequency range and (**d**) the higher-frequency range.

For the initial simulation, we used 3.25 as the permittivity of PET because 3.25 is the measured dielectric constant for 10 GHz, which is the operating frequency for the dielectric constant measurement equipment we used. For the lower-frequency band of 5.5 to 7.5 GHz, the simulation result achieved by setting the permittivity as 3.25 matches well with the measurement result. However, for the higher-frequency band of 20 to 22 GHz, the simulation result achieved by setting the permittivity as 3.25 has a frequency shift of 0.18 GHz. We assumed that this discrepancy results from a mismatch in the permittivity of PET between the simulation value and real value due to the dispersive property of the dielectric constant of PET. Therefore, to find the proper value of the permittivity of PET, we conducted dielectric constant optimization through simulation. As shown in Figure 12, when the permittivity is revised from 3.25 to 2.35, the simulated absorptivity matches better with the measurement result than the initial simulation result. The peak absorption frequency was the same for both the measurement and re-simulation results (21.14 GHz). Through this optimization process, we could figure out how the dielectric constant of PET changes along with an increase in frequency and build a more credible simulation model, overcoming the limitation that meant we could measure the dielectric constant only for 10 GHz among the operation frequency band of the proposed absorber.

Figure 13 displays the simulated absorptivity according to different incident angles ranging from 0 to 60 degrees. The higher absorption frequency varies along with the varying incident angle, while the lower absorption frequency remains consistent. In addition, two or more absorption peaks with 90% absorptivity exist from 4 to 27 GHz for incident angles of 0, 20, 40, and 60 degrees. However, as the absorption frequency changes along with the varying incident angle, the proposed MMA does not have the property of incident angle insensitivity. The reason behind the change in the higher absorption frequency is assumed

to be due to the relatively large electrical size of the unit cell for the high-frequency band, the K-band. Therefore, for future work, we aim to develop an incident angle-insensitive MMA by selecting unit cell geometries that differ in aspects such as subwavelength size [37] or circular sector design [38].

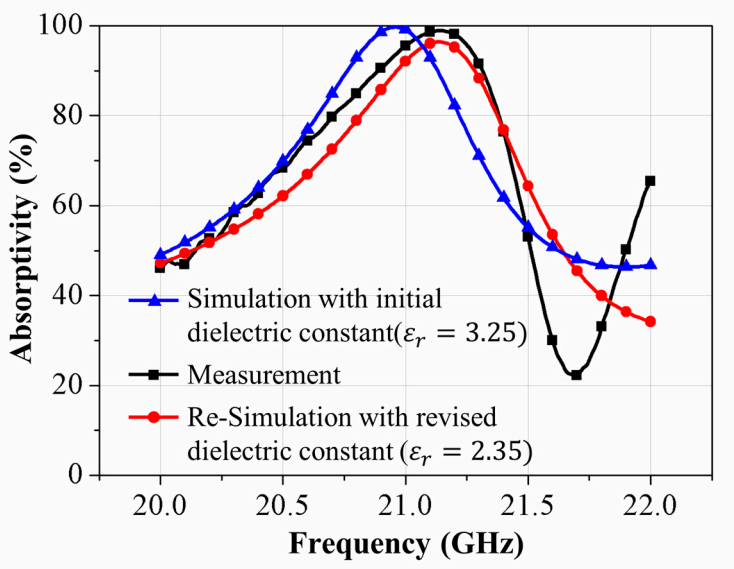

Figure 12. Comparison of the measured and simulated absorptivity with different dielectric constants.

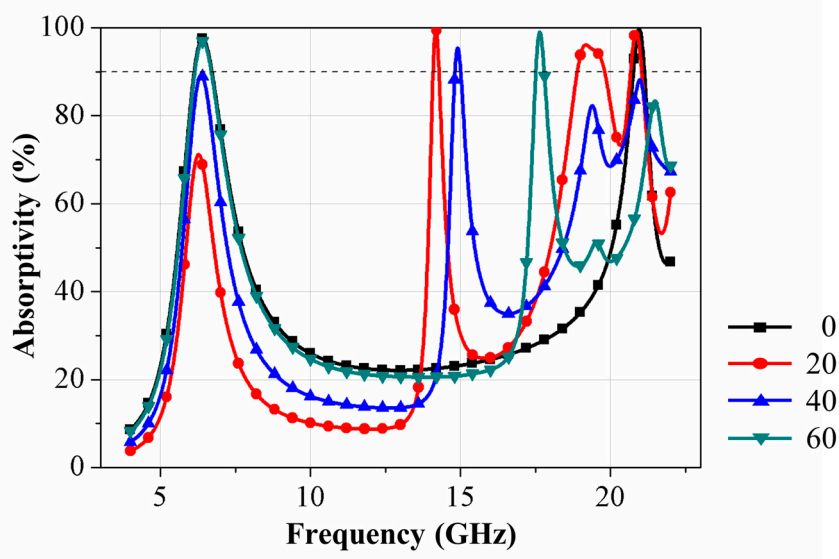

Figure 13. Simulated absorptivity according to different incident angles ranging from 0 to 60 degrees.

A comparison of the proposed dual-band MMA using second-order cross-fractal structures and other fractal-structured MMAs is presented in Table 2. The proposed MMA holds the unique property of optical transparency. Furthermore, what most distinguishes this work from other research is that the proposed MMA was fabricated via a screen printing process. Utilizing screen printing to fabricate a transparent fractal-structured MMA has never been reported before. Screen printing has a very short processing time; therefore, it can be efficiently utilized for mass production, which is advantageous for various practical applications. In addition, as shown in Table 2, the screen printing method has the advantages of low cost and low complexity compared to other common fabrication methods such as lithography and etching and ITO sputtering. Consequently, the proposed MMA not only presents excellent absorption performance and the property of optical

transparency but can also be realized through a fabrication process that is highly efficient in terms of both time and cost, which is highly suitable for wide industrial applications.

Table 2. A performance comparison between previous fractal structured MMAs and the one this work proposes.

Structure Characteristics	Peak Absorption Frequency	Optical Transparency	Process Technology	Cost and Complexity	Ref
Circular fractal structure	2.39 and 4.45 and 12.1 GHz	No	Lithography and Etching	high	[25]
Combination of fractal and circular structure	8.7 and 9.25 and 9.93 GHz	No	Lithography and Etching	high	[23]
Cross-fractal structure and H-shaped fractal structure	6.68 and 12.17 GHz	No	Lithography and Etching	high	[26]
Second-order cross-fractal structure	4.42 and 7.02 GHz	Yes	ITO sputtering	high	[27]
Second-order cross-fractal structure	6.45 and 21.14 GHz	Yes	Screen printing	low	This work

5. Conclusions

Herein, an optically transparent dual-band MMA constituting a second-order cross-fractal-structured unit cell that unprecedentedly employed Ag nanowire screen printing was proposed and experimentally demonstrated. The second-order cross-fractal structure generated two absorption peaks that absorbed 97.48% and 98.92% of the electromagnetic waves at 6.45 and 21.14 GHz, respectively. In addition, the screen printing of transparent conductive ink based on Ag nanowire realized transparency in visible-light wavelengths. As the proposed absorber did not deteriorate the visibility of the environments (due to its transparency), this property extended the potential applications of the proposed electromagnetic absorber to various environments. Particularly, the suggested MMA exhibits near-perfect absorption capabilities within the C- and K-bands, which are military radar frequencies, along with being optically transparent. This allows it to be affixed to the windows of stealth aircraft. Consequently, this MMA is highly suitable for use in radar stealth technologies, offering efficient application possibilities. Regarding our future work, we are currently working on designing an incidence angle-insensitive MMA utilizing the concept of Ag nanowire screen printing, which has been proposed and proven to be effective in this paper.

Author Contributions: Conceptualization, S.L.; methodology, S.B., J.K. and S.L.; software, S.B.; validation, S.B. and J.K.; formal analysis, S.B.; investigation, S.B. and J.K.; resources, S.B. and J.K.; data curation, S.B., M.L. and J.K.; writing—original draft preparation, S.B.; visualization, S.B. and M.L.; supervision, S.L.; project administration, S.L.; funding acquisition, S.L. All authors have read and agreed to the published version of the manuscript.

Funding: This research was supported by a National Research Foundation of Korea (NRF) grant funded by the Korean government (MSIT) (2021R1A2C3005239) and the MSIT (Ministry of Science and ICT), Korea, under the ITRC (Information Technology Research Center) support program (IITP-2024-RS-2022-00156353) supervised by the IITP (Institute for Information & Communications Technology Planning & Evaluation). This research was supported by the Chung-Ang University Graduate Research Scholarship in 2024.

Data Availability Statement: Data are contained within the article.

Conflicts of Interest: The authors declare no conflicts of interest.

References

1. Sun, H.; Gu, C.; Chen, X.; Li, Z.; Liu, L.; Xu, B.; Zhou, Z. Broadband and Broad-Angle Polarization-Independent Metasurface for Radar Cross Section Reduction. *Sci. Rep.* **2017**, *7*, 40782. [CrossRef]
2. Marra, F.; Lecini, J.; Tamburrano, A.; Pisu, L.; Sarto, M.S. Electromagnetic Wave Absorption and Structural Properties of Wide-Band Absorber Made of Graphene-Printed Glass-Fibre Composite. *Sci. Rep.* **2018**, *8*, 12029. [CrossRef]
3. Tong, X. *Advanced Materials and Design for Electromagnetic Interference Shielding*, 1st ed.; Taylor & Francis Group: Boca Raton, FL, USA, 2008.
4. Mishra, R.K.; Gupta, R.D.; Datar, S. Metamaterial Microwave Absorber (MMA) for Electromagnetic Interference (EMI) Shielding in X-Band. *Plasmonics* **2021**, *16*, 2061–2071. [CrossRef]
5. Fante, R.L.; Mccormack, M.T. Reflection Properties of the Salisbury Screen. *IEEE Trans. Antennas Propag.* **1988**, *36*, 1443–1454. [CrossRef]
6. Du Toit, L.J. The Design of Jauman Absorbers. *IEEE Antennas Propag. Mag.* **1994**, *36*, 17–25. [CrossRef]
7. Landy, N.I.; Sajuyigbe, S.; Mock, J.J.; Smith, D.R.; Padilla, W.J. Perfect Metamaterial Absorber. *Phys. Rev. Lett.* **2008**, *100*, 207402. [CrossRef] [PubMed]
8. Li, K.; Lu, H.; Bi, M.; He, W.; Qi, L.; Zhou, Z.; Weng, X. Multi-Band Polarization-Insensitive Metamaterial Absorber for Microwave Based on Slotted Structure and Magnetic Rubber. *Polymers* **2022**, *14*, 1576. [CrossRef] [PubMed]
9. Ma, Y.; Chen, Q.; Grant, J.; Saha, S.C.; Khalid, A.; Cumming, D.R.S. A Terahertz Polarization Insensitive Dual Band Metamaterial Absorber. *Opt. Lett.* **2011**, *36*, 945. [CrossRef] [PubMed]
10. Zhang, N.; Zhou, P.; Cheng, D.; Weng, X.; Xie, J.; Deng, L. Dual-Band Absorption of Mid-Infrared Metamaterial Absorber Based on Distinct Dielectric Spacing Layers. *Opt. Lett.* **2013**, *38*, 1125. [CrossRef] [PubMed]
11. Soheilifar, M.R.; Sadeghzadeh, R.A. Design, Fabrication and Characterization of Stacked Layers Planar Broadband Metamaterial Absorber at Microwave Frequency. *AEU Int. J. Electron. Commun.* **2015**, *69*, 126–132. [CrossRef]
12. Wen, Q.Y.; Zhang, H.W.; Xie, Y.S.; Yang, Q.H.; Liu, Y.L. Dual Band Terahertz Metamaterial Absorber: Design, Fabrication, and Characterization. *Appl. Phys. Lett.* **2009**, *95*, 241111. [CrossRef]
13. Lee, H.M.; Lee, H.S. A Method for Extending the Bandwidth of Metamaterial Absorber. *Int. J. Antennas Propag.* **2012**, *2012*, 859429. [CrossRef]
14. Ajewole, B.; Kumar, P.; Afullo, T. I-Shaped Metamaterial Using SRR for Multi-Band Wireless Communication. *Crystals* **2022**, *12*, 559. [CrossRef]
15. Islam, S.S.; Iqbal Faruque, M.R.; Islam, M.T. Design and Absorption Analysis of a New Multiband Split-S-Shaped Metamaterial. *Sci. Eng. Compos. Mater.* **2017**, *24*, 139–148. [CrossRef]
16. Mandelbrot, B.B.; Wheeler, J.A. The Fractal Geometry of Nature. *Am. J. Phys.* **1983**, *51*, 286–287. [CrossRef]
17. Anguera, J.; Andújar, A.; Jayasinghe, J.; Sameer Chakravarthy, V.V.S.S.; Chowdary, P.S.R.; Pijoan, J.L.; Ali, T.; Cattani, C. Fractal Antennas: An Historical Perspective. *Fractal Fract.* **2020**, *4*, 3. [CrossRef]
18. Bisht, N.; Malik, P.K.; Das, S.; Islam, T.; Asha, S.; Alathbah, M. Design of a Modified MIMO Antenna Based on Tweaked Spherical Fractal Geometry for 5G New Radio (NR) Band N258 (24.25–27.25 GHz) Applications. *Fractal Fract.* **2023**, *7*, 718. [CrossRef]
19. Shan, D.; He, L.; Deng, L.; Luo, H.; Liao, C.; Peng, Y.; Xu, Y.; Huang, S. Comptibility of Optical Transparency and Microwave Absorption in C-Band for the Metamaterial with Second-Order Cross Fractal Structure. *Phys. E Low-Dimens. Syst. Nanostructures* **2020**, *116*, 113756. [CrossRef]
20. Kim, J.; Keun, J.; Yoo, T.; Lim, S. Miniaturization and Bandwidth Enhancement of Fractal-Structured Two-Arm Sinuous Antenna Using Gap Loading with Meandering. *Fractal Fract.* **2023**, *7*, 841. [CrossRef]
21. Paun, M.A.; Nichita, M.V.; Paun, V.A.; Paun, V.P. Minkowski's Loop Fractal Antenna Dedicated to Sixth Generation (6G) Communication. *Fractal Fract.* **2022**, *6*, 402. [CrossRef]
22. Vallappil, A.K.; Khawaja, B.A.; Rahim, M.K.A.; Uzair, M.; Jamil, M.; Awais, Q. Minkowski–Sierpinski Fractal Structure-Inspired 2 × 2 Antenna Array for Use in Next-Generation Wireless Systems. *Fractal Fract.* **2023**, *7*, 158. [CrossRef]
23. Fan, S.; Song, Y. Bandwidth-Enhanced Polarization-Insensitive Metamaterial Absorber Based on Fractal Structures. *J. Appl. Phys.* **2018**, *123*, 085110. [CrossRef]
24. Munaga, P.; Ghosh, S.; Bhattacharyya, S.; Srivastava, K.V. A Fractal-Based Compact Broadband Polarization Insensitive Metamaterial Absorber Using Lumped Resistors. *Microw. Opt. Technol. Lett.* **2016**, *58*, 343–347. [CrossRef]
25. Jiang, H.; Xue, Z.; Li, W.; Ren, W. Multiband Polarisation Insensitive Metamaterial Absorber Based on Circular Fractal Structure. *IET Microw. Antennas Propag.* **2016**, *10*, 1141–1145. [CrossRef]
26. Fang, S.; Deng, L.; Zhang, P.; Qiu, L.; Xie, H.; Du, J.; Wang, H.; Zhao, H. Dual-Band Metamaterial Absorber with Stable Absorption Performance Based on Fractal Structure. *J. Phys. D Appl. Phys.* **2022**, *55*, 095003. [CrossRef]
27. Peng, Y.; Wang, Q.; Xu, Y.; Shan, D.; He, L.; Cao, Y. Optically Transparent and Mechanically Stretchable Fractal-Structured Wave-Absorbing Metamaterial in Low Frequency Range. *J. Alloys Compd.* **2023**, *961*, 171100. [CrossRef]
28. Nguyen, T.D.; Kim, S.E.; Jung, C.W. Compact, Flexible and Transparent Antenna Using MMF for Conformal Wi-Fi 7 Applications. *J. Electr. Eng. Technol.* **2023**, *18*, 4341–4352. [CrossRef]
29. Nguyen, T.D.; Choi, J.H.; Jung, C.W. Optically Transparent Patch Antennas Using Saltwater for WLAN Applications. *J. Electromagn. Eng. Sci.* **2022**, *22*, 609–615. [CrossRef]

30. Phan, D.T.; Jung, C.W. Transparent Liquid Multiple-Antenna Array with a High Gain and Beam Diversity for UHD TV Applications. *J. Electromagn. Eng. Sci.* **2022**, *22*, 186–194. [CrossRef]
31. Zhang, C.; Cheng, Q.; Yang, J.; Zhao, J.; Cui, T.J. Broadband Metamaterial for Optical Transparency and Microwave Absorption. *Appl. Phys. Lett.* **2017**, *110*, 143511. [CrossRef]
32. Kang, J.; Qu, Z.; Duan, J.; Jing, H.; Hao, J.; Song, C.; Wang, J.; Zhang, B. Multispectral Flexible Ultrawideband Metamaterial Absorbers for Radar Stealth and Visible Light Transparency. *Opt. Mater.* **2023**, *135*, 113351. [CrossRef]
33. Jiang, H.; Yang, W.; Lei, S.; Hu, H.; Chen, B.; Bao, Y.; He, Z. Transparent and Ultra-Wideband Metamaterial Absorber Using Coupled Hexagonal Combined Elements. *Opt. Express* **2021**, *29*, 29439. [CrossRef]
34. Nguyen, T.D.; Lee, Y.; Jung, C.W. Transparent and Flexible Patch Antenna Using MMF for Conformal WiFi-6E Applications. *J. Electromagn. Eng. Sci.* **2023**, *23*, 310–317. [CrossRef]
35. Yoo, Y.; Jeong, H.; Lim, D.; Lim, S. Stretchable Screen-Printed Metasurfaces for Wireless Strain Sensing Applications. *Extrem. Mech. Lett.* **2020**, *41*, 100998. [CrossRef]
36. Hollis, J.S.; Ecker, H.A. Determination of Far-Field Antenna Patterns from Near-Field Measurements. *Proc. IEEE* **1973**, *61*, 1668–1694. [CrossRef]
37. Yoo, M.; Kim, H.K.; Lim, S. Angular- and Polarization-Insensitive Metamaterial Absorber Using Subwavelength Unit Cell in Multilayer Technology. *IEEE Antennas Wirel. Propag. Lett.* **2016**, *15*, 414–417. [CrossRef]
38. Lee, D.; Hwang, J.G.; Lim, D.; Hara, T.; Lim, S. Incident Angle- and Polarization-Insensitive Metamaterial Absorber Using Circular Sectors. *Sci. Rep.* **2016**, *6*, 27155. [CrossRef] [PubMed]